## PAPER

Check for updates

# Electronic and magnetic properties of defective and Fe-doped InS monolayers adjusted by hole doping as a second functionalization step: a first-principles study

Nguyen Thanh Tien, [ID] [a] Nguyen Thanh Son,[b] Truong Tuan Vu,[acd] R. Ponce-Pérez,[e] J. Guerrero-Sanchez[e] and D. M. Hoat [ID] *[cd]

In this work, hole doping is proposed as a second functionalization step to modify the electronic and magnetic properties of defective and Fe-doped InS monolayers. The pristine monolayer is confirmed to be a two-dimensional (2D) material with an indirect gap of 1.65 eV, whose In–S chemical bonds exhibit both covalent and ionic characters. The creation of a single In vacancy ($1Va_{In}$) or a pair of In vacancies ($2Va_{In}$) induces half-metallicity in the InS monolayer. In these cases, total magnetic moments of 1.00 and $2.00\mu_B$, respectively, are obtained, where S atoms closest to defect sites produce primarily the system magnetic moments. Meanwhile a single S vacancy ($1Va_S$) induces no magnetism, however this defect causes a band gap reduction of the order of 28.48%. Significant magnetism is also obtained by Fe doping ($Fe_{In}$) with an overall moment of $5.00\mu_B$, originating primarily from the transition metal impurity. Moreover, a magnetic semiconductor nature is also developed in the InS monolayer through doping with an Fe atom. The in-plane magnetic anisotropy (IMA) is confirmed for the magnetic $1Va_{In}$@mo, $2Va_{In}$@mo, and $Fe_{In}$@mo systems. Further, the pristine InS monolayer is magnetized with a hole concentration of 1.5 holes per supercell. Both the magnetization and IMA of the $1Va_{In}$@mo system can be significantly enhanced by hole doping, while the magnetism in the $2Va_{In}$@mo system disappears upon adding a hole in its lattice. The nonmagnetic $1Va_S$@mo system becomes magnetic when it has been hole-doped with total magnetic moment up to $0.89\mu_B$. It is found that hole doping enhances the IMA of the $Fe_{In}$@mo system, despite its magnetic moment reducing. In addition, the electronic structures of the considered InS systems can be effectively controlled by hole doping, where the hole level plays a key role. Our findings pave a solid way to functionalize the InS monolayer towards diverse spintronic and optoelectronic applications.

## 1. Introduction

Since the successful isolation of graphene,[1] two-dimensional (2D) crystalline structures have been attracting enormous research attention from the scientific community. Intriguing properties such as high carrier mobility derived from its Dirac cone with linear energy dispersion, high mechanical strength, and large surface area, *etc.* have been found for graphene,[2,3]

making it the most studied 2D material. However, graphene is intrinsically a semimetal, not a semiconductor with an intrinsic band gap, such that its use in electronic nanodevices is considerably hindered. To overcome this limitation, different band gap opening strategies have been proposed through chemical modification[4,5] or edge controlling.[6,7] Simultaneously, researchers have also devoted extensive efforts to the continuous discovery of new 2D alternative materials. Consequently, a large variety of 2D families have been explored experimentally and theoretically, including transition metal dichalcogenides (TMDs)[8,9] and nitrides/carbides (MXenes),[10,11] pnictogens,[12,13] and II–VI group[14,15] and III–VI group materials,[16,17] *etc.* Exceptional physical and chemical properties endow the 2D materials with promise for diverse applications in catalysis,[18,19] optoelectronics, electronics, and photonics,[20,21] photovoltaics,[22,23] energy storage,[24,25] and spintronics,[26,27] *etc.*

In the past years, atomically thin III-group monochalcogenides (III–X; III = Al, Ga, and In; X = S, Se, and Te) have

*[a]College of Natural Sciences, Can Tho University, 3-2 Road, Can Tho City 900000, Vietnam*

*[b]Center of Scientific Research and Application, Lac Hong University, No. 10 Huynh Van Nghe Str, Tran Bien Ward, Dong Nai Province, Vietnam*

*[c]Institute of Theoretical and Applied Research, Duy Tan University, Ha Noi 100000, Vietnam. E-mail: dominhhoat@duytan.edu.vn*

*[d]School of Engineering and Technology, Duy Tan University, Da Nang 550000, Vietnam*

*[e]Universidad Nacional Autónoma de México, Centro de Nanociencias y Nanotecnología, Apartado Postal 14, Ensenada, Baja California, Código Postal 22800, Mexico*

been prepared successfully in experiments using either top-down exfoliation from their bulk counterpart[28,29] or bottom-up chemical vapor deposition (CVD),[30,31] providing opportunity to study their properties. These 2D III–X members are semiconductors with relatively large band gaps, exhibiting strong absorption in the UV-vis regime and promising photodetection performance.[16,32] Particularly, the first successful synthesis of large-area indium sulfide (InS) atomic layers was reported by Tu et al.[33] using the CVD method. The fabricated InS field-effect transistors (FETs) exhibit n-type transport behavior and have an on/off current ratio exceeding $10^3$. Using first-principles calculations, several groups have investigated the electronic modification of the InS monolayer through strain engineering[34,35] and the formation of heterostructures.[36,37] Moreover, the adsorption and doping with transition metals have been predicted to induce significant magnetism in the InS monolayer, making it suitable for spintronic applications.[38,39]

On the other hand, the majority of the discovered 2D materials have no intrinsic magnetism, raising a great challenge to induce and control the magnetism in 2D materials towards opening new functionalities. In this regard, vacancy defects have been widely explored to create magnetic moment and alter the electronic structure of 2D materials. For example, the theoretical study of Ao et al.[40] has asserted that Ga vacancies in the GaSe monolayer gives a total magnetic moment of between 1.00 and $4.00\mu_B$, while the band gap narrowing is achieved by a single Se vacancy. Similar effects of native vacancy defects have been found for the GaS monolayer.[41] In addition, carrier doping has been also explored as an effective way to modify the 2D materials' electronic and magnetic properties. For example, Meng et al.[42] have demonstrated the emergence of half-metal behavior in nonmagnetic metal oxide monolayers MO (M = Ga and In) induced by hole doping. Similarly, a magnetic moment up to $1.00\mu_B$ with the half-metal state can be achieved for the GaSe monolayer, depending on the hole level.[43]

To the best of our knowledge, the effects of vacancy defects, Fe doping and hole doping, as well as their coeffects on the InS monolayer's electronic and magnetic properties have not been investigated well, so far. In this work, our main aim is to report new results to rectify this gap in the research. To achieve this goal, a $4 \times 4 \times 1$ supercell of the InS monolayer is generated to model a single In vacancy, a pair of In vacancies, a single S vacancy, and Fe doping. Moreover, different hole levels of 0.5, 1.0, and 1.5 holes per supercell are considered for all the perfect, defective, and doped systems. Our results demonstrate the effectiveness of using defects, doping and hole doping to alter and control the electronic and magnetic properties of the InS monolayer, which can be useful theoretical guidance for the field of 2D materials.

## 2. Computational details

Within the framework of density functional theory (DFT),[44] spin-polarized calculations are performed using the projector augmented wave (PAW) method and Perdew–Burke–Ernzerhof-parameterised generalized gradient approximation (GGA-PBE)

as implemented in Vienna ab initio simulation package (VASP).[45–47] Despite the well-known band gap underestimation, the PBE functional can describe very well the variation trends of the band gap and magnetic moment of the perfect and defective InS monolayer upon hole doping. In addition, the DFT+U method with an effective Hubbard parameter of 5.40 eV (ref. 48 and 49) is also adopted to treat properly the high-correlation effects of Fe-3d electrons. For the plane-wave expansion of the electronic wave function, the cutoff energy is set to 500 eV. k-Point grids of $20 \times 20 \times 1$ and $4 \times 4 \times 1$ are generated using the Monkhorst–Pack method[50] to sample the Brillouin zone of the InS unit cell and supercell, respectively. The relaxation of geometry structures is realized until the force acting on each In and S atom is less than $1 \times 10^{-2}$ eV Å$^{-1}$. The convergence criterion of self-consistency for energy is set to $1 \times 10^{-6}$ eV. In all cases, a vacuum space with width more than 19 Å is placed along the z-axis to eliminate the interaction between periodic monolayer images along the perpendicular direction, where the monolayer systems are expanded in the xy-plane. It is important to mention that the spurious Coulombic interactions can be corrected by using a uniformly scaled supercell with equal lateral sizes ($L_{xx} = L_{yy} = L_{zz}$), which is a proven method from previous studies.[51–55] However, for the $4 \times 4 \times 1$ supercell, the correction can be achieved with a special vacuum $L_z^s$ of about 16 Å.[56] Therefore, it can be expected that the vacuum gap inserted in our structural models is reasonable and produces reliable results.

The formation energy $E_f$ values of the defective and doped InS systems are calculated using the following expression:

$$E_f = \frac{E_{X@mo} - E_{mo} + \sum_i n_i \mu_i - \sum_j n_j \mu_j}{\sum_i n_i} \quad (1)$$

where $E_{X@mo}$ and $E_{mo}$ are the total energy of the defective/doped system and pristine InS monolayer (X refers to the type of vacancy and doping), respectively; $n_i$ ($i$ = In and S) and $n_j$ ($j$ = Fe) denote the number of removed In/S atoms and incorporated impurity atoms, respectively, $\mu$ is the chemical potential of the atom. Cohesive energy $E_c$ is also computed as follows:

$$E_c = \frac{E_{X@mo} - m_{In}E_{In} - m_S E_S - m_{Fe}E_{Fe}}{m_{In} + m_S + m_{Fe}} \quad (2)$$

herein, $m_{atom}$ and $E_{atom}$ denote the number of atoms in the defective/doped system and the energy of the isolated atom, respectively.

The magnetic anisotropy of the magnetic InS-based systems is studied by calculating the magnetic anisotropy energy (MAE) as follows:

$$MAE = E[100] - E[001] \quad (3)$$

where the total system energies $E[100]$ and $E[001]$ are computed using a two-step approach: (1) self-consistent calculations without spin–orbit coupling (SOC) to determine the converged charge density, followed by (2) non-self-consistent calculations with SOC and setting the easy magnetization axis along the in-plane [100] and out-of-plane [001] direction, respectively.

# 3. Results and discussion

## 3.1. Stability and electronic properties of InS monolayer

A $4 \times 4 \times 1$ supercell of the InS monolayer at equilibrium is visualized in Fig. 1a. Note that the atomic structure is composed by S–In–In–S atomic sublayer stacking, in which two In sub-layers are vertically bound and aligned. The vertical alignment is also observed for two S sublayers. From the top-view, In and S atoms are situated in a graphene-like honeycomb configuration. After the structural relaxation, the following parameters for the InS monolayer unit cell are obtained: (1) lattice constant $a = 3.94$ Å; (2) chemical bond lengths $d_{In-S} = 2.57$ Å and $d_{In-In} = 2.82$ Å, which are in good agreement with previous studies;[57] (3) total structural buckling height $\Delta_t = 2 \times \Delta_{In-S} + \Delta_{In-In} = 2 \times 1.19 + 2.82 = 5.20$ Å; and (4) interatomic angles $\angle SInS = 100.29°$ and $\angle SInIn = 117.57°$. In the following, the stability of the InS monolayer is analyzed.

• Adopting the finite displacement method, we calculate the phonon dispersion curves of the InS monolayer with the help of the PHONOPY code.[58] Results given in Fig. 2a confirm good dynamical stability for the studied InS monolayer, considering the absence of nonphysical imaginary frequencies in its phonon spectra.

• *Ab initio* molecular dynamics (AIMD) simulations are carried out to examine the InS monolayer thermal stability, using a canonical ensemble and Nosé–Hoover thermostat.[59,60] Output is recorded for total time of 5 ps with time steps of 2 fs. From Fig. 1b, we can see that after 5 ps of AIMD simulations, constituent In and S atoms displace slightly from their equilibrium. Importantly, no structural reconstruction is produced, such that the initial atomic configuration is well preserved. In
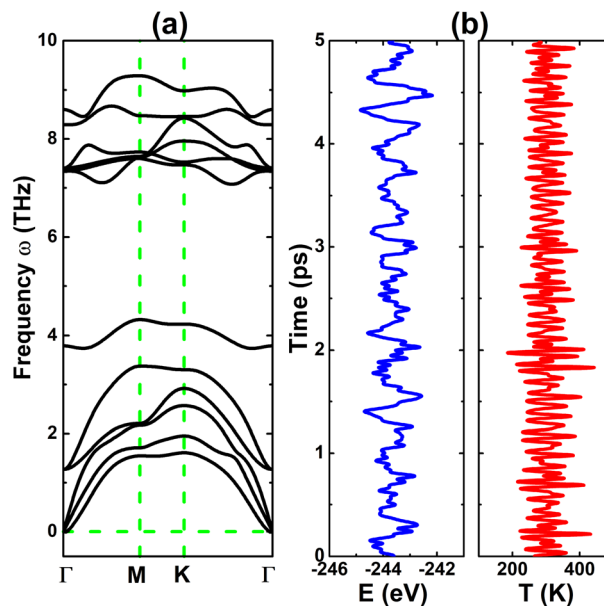


Fig. 2  (a) Phonon dispersion curves and (b) AIMD simulations at 300 K (fluctuation of $E$ – energy and $T$ – temperature) of the InS monolayer.

addition, the energy and temperature parameters exhibit stable fluctuation within a small range during AIMD simulations as observed in Fig. 2b. These results confirm that the InS monolayer is thermally stable.

• To verify the mechanical stability, we calculate the elastic constants $C_{11}$ and $C_{12}$ of the InS monolayer, which can describe the elasticity because of the 2D hexagonal symmetry. According to our simulations, these constants are calculated to be 57.26 and 16.64 N m$^{-1}$, respectively. Importantly, these values satisfy that $C_{11} > 0$ and $C_{11} > |C_{12}|$, which have been proposed to determine the mechanical stability.[61] These results confirm that the InS monolayer is mechanically stable.

Using the optimized unit cell, we calculate the InS monolayer electronic band structure. Results are plotted in Fig. 3a with the orbital-decomposed contribution of each atom. The Mexican-hat-like energy dispersion around the Fermi level can be observed, giving the indirect gap of this 2D material. Our calculations provide an energy gap of 1.65 eV for the InS monolayer, which agrees well with previous studies.[16] Note that this gap is determined by the upper valence band originated from In-p$_z$/S-p$_z$ states and the lower conduction band formed mainly by the In-s state. Moreover, the In-s and S-p$_{x,y,z}$ states also make contributions to the lower part of the valence band, meanwhile the In-p$_{x,y,z}$ states build mainly the upper part of the conduction band. In order to get a more accurate band gap for the InS monolayer, the hybrid functional HSE06 with a 25% fraction of the exact Hartree exchange potential is adopted.[62] Our HSE06-based calculations provide a band gap of 2.49 eV that is larger than that obtained using the PBE functional, however both functionals produce quite similar band structure profiles with indirect-gap semiconductor character (see Fig. S1 in the SI file). The band structure profiles also assert the hybridization of In-belonging and S-belonging electronic states,
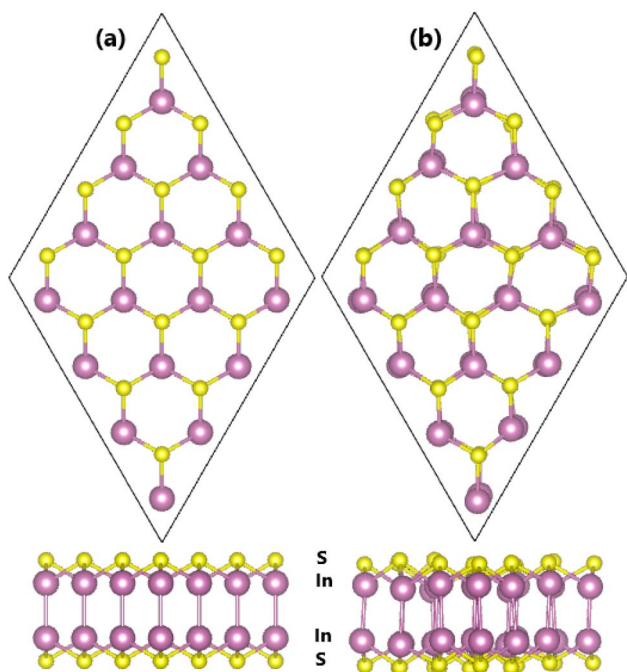


Fig. 1  Atomic structure in a $4 \times 4 \times 1$ supercell of the InS monolayer (a) before (optimized) and (b) after AIMD simulations.
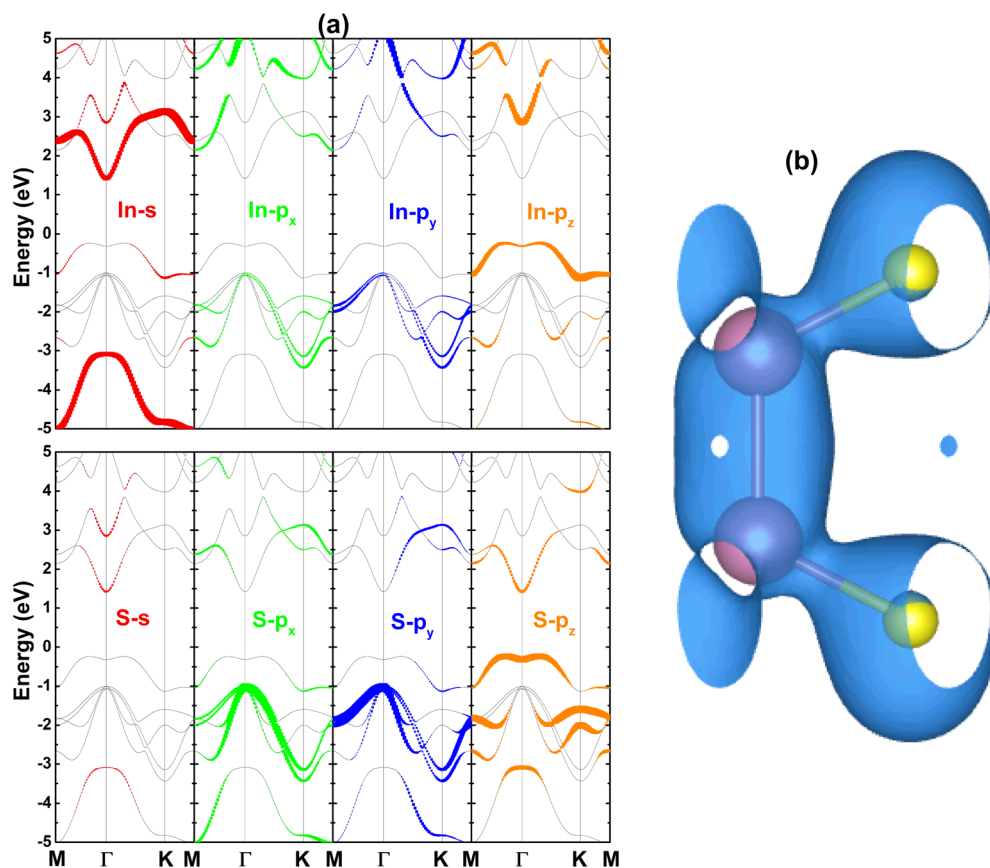
**Fig. 3** (a) Projected band structure (the Fermi level is set to 0 eV) and (b) electron localization function (iso-surface level: 0.6 e $\text{Å}^{-3}$) of the InS monolayer.

suggesting a covalent In–S bond. This feature is also confirmed by the charge accumulation between In and S atoms as observed in the electron localization function visualized in Fig. 3b. Similarly, the interaction between In–In atoms is predominantly covalent as confirmed by the large charge accumulations between them. However, it is flawed to not consider the ionic character of the In–S chemical bond since the chemical bonds in 2D compounds are not purely covalent because of the difference in electronegativity. To quantitatively study this interaction, the Bader charges of the In and S atoms are analyzed. It is found that each S atom attracts a charge quantity of 0.74$e$ from In atoms. These results confirm the mix of covalent and ionic characters in the In–S bond in the InS monolayer.

### 3.2. Effects of vacancy defects

In this part, the effects of a single In vacancy, a pair of In vacancies, and a single S vacancy on the InS monolayer's electronic and magnetic properties are studied. The defective systems are denoted by $1\text{Va}_{\text{In}}$@mo, $2\text{Va}_{\text{In}}$@mo, and $1\text{Va}_{\text{S}}$@mo, respectively. The formation energies of these systems are calculated to be 3.64, 3.57, and 2.20 eV per atom, respectively. Note that the creation of the S vacancy requires less energy than In vacancies. In addition, the structural–chemical stability of defective InS monolayers is confirmed by the negative $E_{\text{c}}$ values of −3.39, −3.40, and −3.35 eV per atom, respectively.

Our spin-polarized calculations provide overall magnetic moments of 1.00 and 2.00$\mu_{\text{B}}$ for the $1\text{Va}_{\text{In}}$@mo and $2\text{Va}_{\text{In}}$@mo systems, respectively. These results assert the magnetization of the InS monolayer induced by creating In vacancies. To further study the magnetism origin, the spin density is illustrated in Fig. 4. This parameter measures the difference in charge density distributed in spin channels that originates the magnetism. From the figure, it can be seen that the magnetic properties of the $1\text{Va}_{\text{In}}$@mo and $2\text{Va}_{\text{In}}$@mo systems are produced mainly by S atoms around vacancy sites, considering the spin iso-surface centered at their sites. Moreover, negative MAE values of −9.89 and −42.99 μeV are obtained for these magnetic systems, respectively, indicating their in-plane magnetic anisotropy (IMA). The more negative MAE value demonstrates that the pair of In vacancies induces stronger IMA than the single In vacancy. In contrast, the single S vacancy preserves the InS monolayer nonmagnetic nature as confirmed by the zero magnetic moment of the $1\text{Va}_{\text{S}}$@mo system. Fig. 5 shows the spin-resolved band structure of the defective InS monolayers. The spin polarization around the Fermi level for the $1\text{Va}_{\text{In}}$@mo and $2\text{Va}_{\text{In}}$@mo systems can be noted . One of their spin states exhibits semiconductor character with energy gaps of 1.44 and 0.19 eV, respectively. Meanwhile, metallic character is obtained in the other spin state. These results confirm that half-metallicity in the InS monolayer is induced by creating In
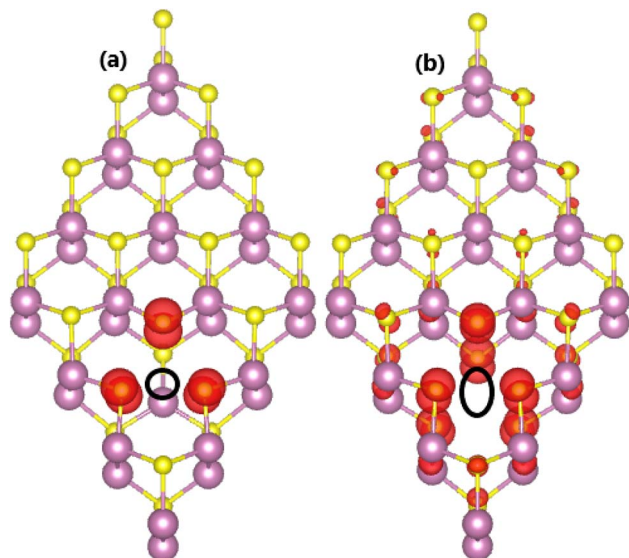
**Fig. 4** Spin density in the InS monolayer with (a) a single In vacancy and (b) a pair of In vacancies (vacancies are marked with black color; iso-surface value: 0.002 e Å$^{-3}$).

vacancies. Along with the confirmed IMA, the magnetic $1Va_{In}$@mo and $2Va_{In}$@mo systems may hold promise for magnetic field sensing applications. In contrast, the nonmagnetic nature of the $1Va_S$@mo system is also reflected in its spin-symmetric band structure profile. In this case, the mid-gap flat subbands cause the band gap reduction to 1.18 eV that corresponds to a reduction of 28.48%. Therefore, it can be concluded that the creation of a single S vacancy may widen the light absorption range of the InS monolayer, making it more suitable for optoelectronic applications.

To get more insights into the atom contributions, the projected density of states (PDOS) spectra of the defective InS monolayers are given in Fig. 6. Note that the magnetism and half-metallicity of the magnetic $1Va_{In}$@mo and $2Va_{In}$@mo systems are determined primarily by S-$p_{x,y,z}$ and In-$p_z$ states since they build mainly the strongly spin-polarized subband structure around the Fermi level. In the case of the $1Va_S$@mo system, the flat subband below the Fermi level is originated mainly from S-$p_z$ and In-$p_z$ states, while the lower conduction band part is formed mainly by the In-s state. These mentioned electronic states are responsible for the band gap reduction as analyzed above.

### 3.3. Effects of Fe doping

The effects of Fe doping on the InS monolayer's electronic and magnetic properties are investigated herein. The Fe-doped InS system is denoted by $Fe_{In}$@mo. From the calculation of formation energy, it is found that an energy quantity of 0.80 eV per atom is required to realize the Fe doping in the InS mono-layer. Moreover, the $Fe_{In}$@mo system has a negative cohesive energy of −3.44 eV per atom that suggests its good structural–chemical stability.

The interaction between the Fe impurity and the host InS monolayer is studied through charge density difference $\Delta\rho$ as follows: $\Delta\rho = \rho(Fe_{In}@mo) - \rho(mo) - \rho(Fe)$, where the terms in the right-hand side refer to the charge density of the doped system, InS monolayer system, and single Fe atom, respectively. From the illustration in Fig. 7a, it can be seen that charge is depleted from the Fe impurity as represented by green iso-surfaces, meanwhile its nearest neighboring S atoms exhibit charge enrichment as indicated by orange iso-surfaces. The $\Delta\rho$ profile suggests charge transfer from the Fe impurity to the host InS monolayer. To quantify the process, Bader charge analysis is performed, which asserts that the host InS monolayer attracts a charge quantity of $0.87e$ from the Fe impurity. These results satisfy the rule of electronegativity since the Fe atom is surrounded by the more electronegative S atoms. In addition, an
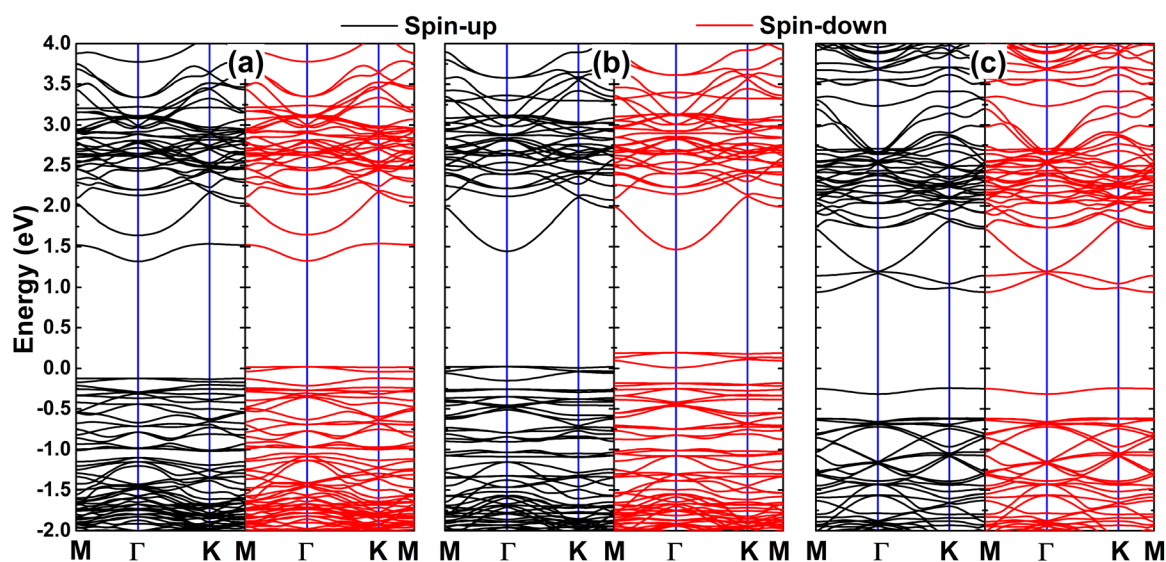


**Fig. 5** Spin-resolved band structure of the InS monolayer with (a) a single In vacancy, (b) a pair of In vacancies, and (c) a single S vacancy (the Fermi level is set to 0 eV).
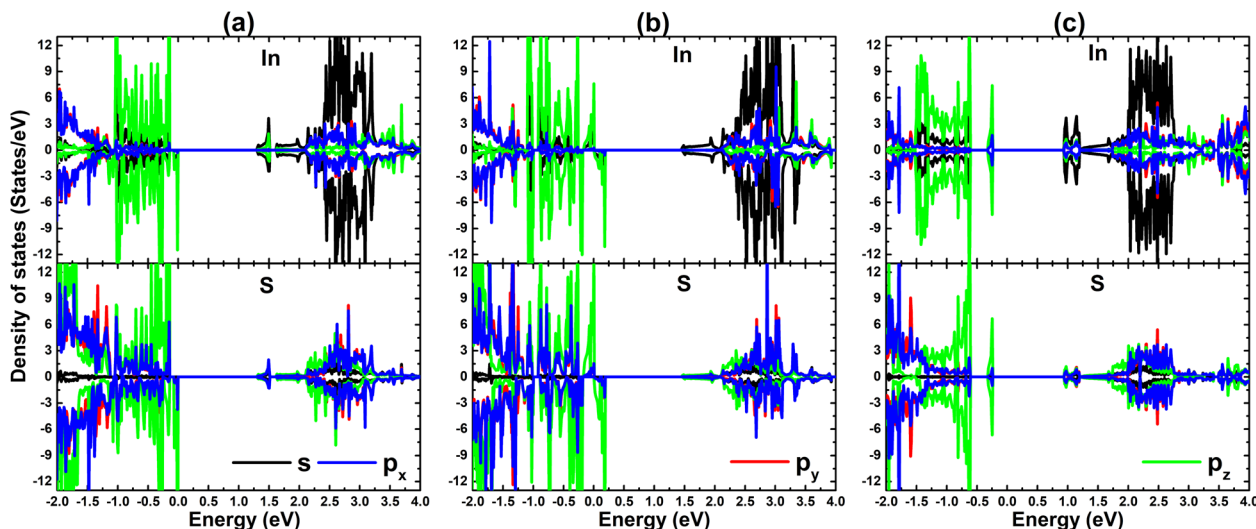
**Fig. 6** Spin-resolved projected density of states of the InS monolayer with (a) a single In vacancy, (b) a pair of In vacancies, and (c) a single S vacancy (the Fermi level is set to 0 eV).
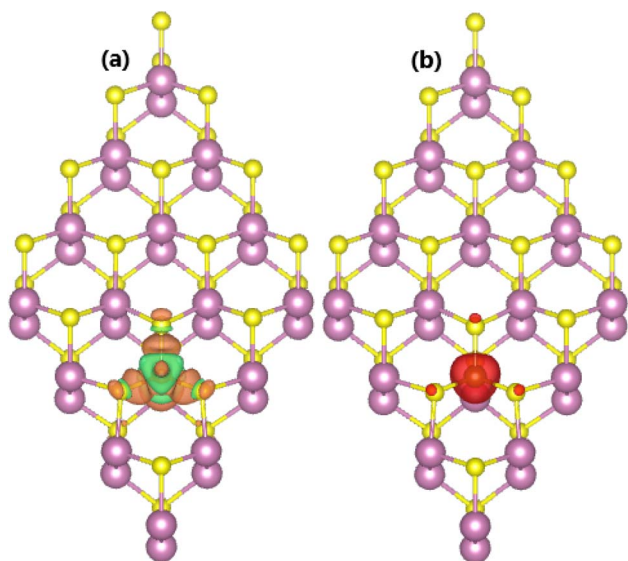


**Fig. 7** (a) Charge density difference (iso-surface value: 0.005 e $Å^{-3}$; green iso-surface: charge depletion; orange iso-surface: charge enrichment) and (b) spin density (iso-surface value: 0.01 e $Å^{-3}$) in the Fe-doped InS monolayer.

overall magnetic moment of $5.0\mu_B$ is obtained for the $Fe_{In}$@mo system, confirming the magnetization of the InS monolayer upon doping with the Fe impurity. The spin density visualized in Fig. 7b shows the main contribution to the system magnetic moment is from the Fe atom since a large spin iso-surface is centered at its site. The local magnetic moment of the Fe impurity is calculated to be $3.72\mu_B$. Moreover, IMA in the InS monolayer induced by the Fe doping is found considering the negative MAE value of $-176.24$ μeV of the $Fe_{In}$@mo system, which is much stronger than the IMA in the defective systems analyzed above. Such that Fe doping may functionalize the InS monolayer towards magnetic field sensing applications.

Fig. 8 shows the spin-resolved band structure of the $Fe_{In}$@mo system, and the PDOS spectra of the Fe impurity and its nearest neighboring S and In atoms are also given to analyze the origin of the mid-gap subbands. From panels a-1 and b-1, diverse flat energy curves either below (in the spin-up channel) or above (in the spin-down channel) the Fermi level can be observed. Importantly, Fe doping induces the magnetic semiconductor nature in the InS monolayer with spin-up and spin-down gaps of 1.01 and 1.34 eV, respectively. The flat mid-gap energy curves are originated mainly from the $Fe-d_{z^2}$ state, where small contributions from the $S-p_z$, In-s, and $In-p_z$ states are also observed. Moreover, $Fe-d_{xy}–d_{yz}–d_{xz}–d_{x^2-y^2}$ states also participate in the formation of the spin-down conduction band of the $Fe_{In}$@mo system.

### 3.4. Effects of hole doping

Now, effects of hole doping on the electronic and magnetic properties of the pristine, defective, and doped InS systems are studied. In a $4 \times 4 \times 1$ supercell, hole concentrations of 0.5, 1.0, and 1.5 (hole) are added. Then, the variations in the magnetic moment, magnetic anisotropy, and electronic band structure are analyzed. The obtained results are summarized in Table 1.

Fig. 9 shows the variation in total magnetic moment as a function of hole concentration. It can be seen that the pristine InS monolayer is magnetized only with 1.5 holes per supercell, for which a value of $0.66\mu_B$ is obtained. Our calculations also assert the IMA of the hole-doped InS monolayer with a negative MAE value of $-8.26$ μeV. The magnetism of the $1Va_{In}$@mo system can be significantly enhanced by hole doping since its magnetic moment is increased and the IMA becomes stronger (with a MAE value up to $-127.76$ μeV obtained with 1.5 holes per supercell) with increasing the hole level. In contrast, the magnetization induced by a pair of In vacancies is made weaker with hole doping since the total magnetic moment decreases from 2.00 to $0.96\mu_B$, and the magnetism disappears when the
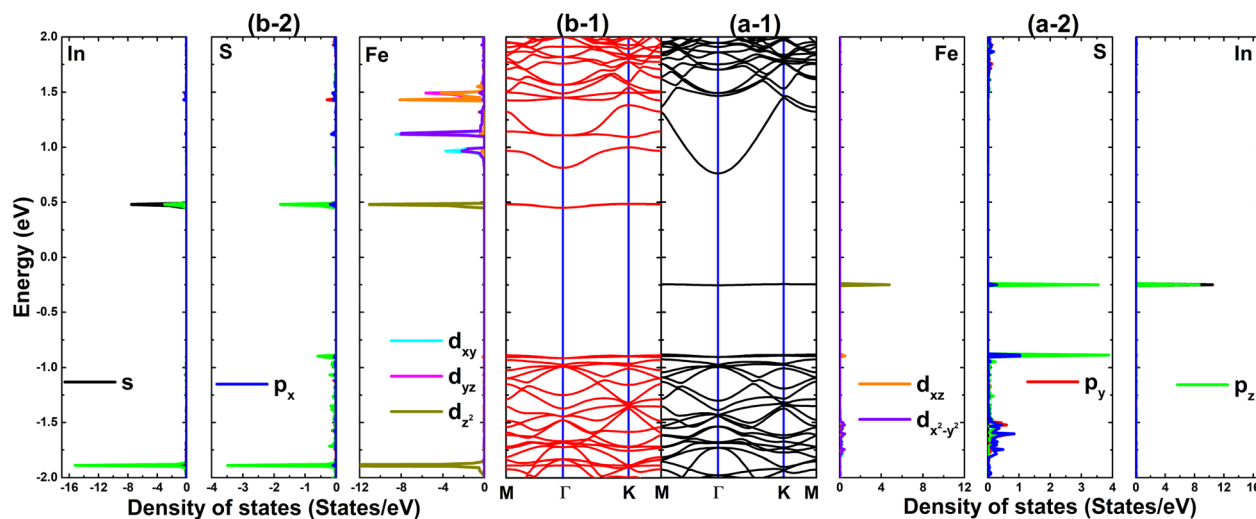
**Fig. 8** Spin-resolved band structure and projected density of states of the Fe impurity and its nearest neighboring S/In atoms: (a1 and a2) spin-up and (b1 and b2) spin-down states (the Fermi level is set to 0 eV).

hole level is 1.0 hole per supercell. Moreover, the IMA of the $2Va_{In}$@mo system becomes weaker considering the less negative MAE value up to 0.5 holes per supercell. As analyzed above, a single S vacancy induces no magnetism in the InS monolayer, however further adding holes in the $1Va_S$@mo system can lead to the appearance of magnetism. Specifically, total magnetic

**Table 1** Total magnetic moment $M_t$ ($\mu_B$), magnetic anisotropy energy MAE ($\mu$eV), and spin-dependent band gap $E_g$ (eV; spin-up/spin-down) of the pristine, defective, and Fe-doped InS monolayers at different hole concentrations

| | Hole concentration | | | |
|---|---|---|---|---|
| | 0.0 | 0.5 | 1.0 | 1.5 |
| **pris@mo** | | | | |
| $M_t$ | 0.00 | 0.00 | 0.00 | 0.66 |
| MAE | | | | −8.26 |
| $E_g$ | 1.65/1.65 | 1.66/1.66 | 1.67/1.67 | 1.68/M |
| **$1Va_{In}$@mo** | | | | |
| $M_t$ | 1.00 | 1.50 | 1.98 | 2.42 |
| MAE | −9.89 | −38.99 | −84.82 | −127.76 |
| $E_g$ | 1.44/M | 1.50/M | 1.52/M | 1.54/M |
| **$2Va_{In}$@mo** | | | | |
| $M_t$ | 2.00 | 0.96 | 0.00 | 0.00 |
| MAE | −42.99 | −8.77 | | |
| $E_g$ | M/0.19 | M/M | M/M | M/M |
| **$1Va_S$@mo** | | | | |
| $M_t$ | 0.00 | 0.46 | 0.89 | 0.68 |
| MAE | | −14.42 | −37.42 | −8.85 |
| $E_g$ | 1.18/1.18 | 1.23/M | 1.24/M | M/M |
| **$Fe_{In}$@mo** | | | | |
| $M_t$ | 5.00 | 4.50 | 4.00 | 3.86 |
| MAE | −176.24 | −171.80 | −205.78 | −215.43 |
| $E_g$ | 1.01/1.34 | M/1.01 | 0.23/0.69 | 0.74/0.27 |

moments between 0.46 and 0.89$\mu_B$ can be obtained with the IMA confirmed by negative MAE values between −37.42 and −8.85 $\mu$eV. Interestingly, opposite trends are noted for the magnetic moment and IMA of the $Fe_{In}$@mo system. Specifically, the magnetic moment decreases upon increasing the hole concentration, meanwhile the IMA can be enhanced significantly since the MAE value becomes much more negative with hole concentrations up to 1.5 holes per supercell. Such that hole doping may be an efficient method to consolidate the application of the $Fe_{In}$@mo system in magnetic field sensing.

From Table 1, it can be seen that the pristine InS monolayer preserves its nonmagnetic semiconductor nature with hole doping, however it becomes a half-metallic 2D system at a hole concentration of 1.5 holes per supercell. In the case of $1Va_{In}$@mo, half-metallicity is obtained regardless of hole concentration level. Meanwhile, the hole doping is found to metallize the $2Va_{In}$@mo system, since both of its spin states exhibit metallic character. Upon hole doping, the feature-rich half-metallicity is induced in the $1Va_S$ system, however
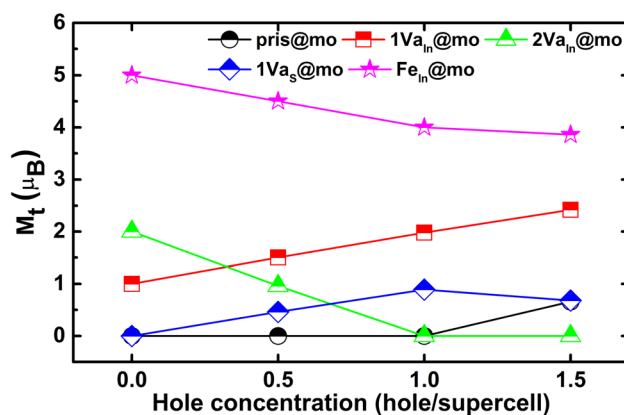


**Fig. 9** Total magnetic moment of the pristine, defective, and Fe-doped InS monolayers at various hole concentrations.

metallization of the system takes place at a high hole concentration of 1.5 holes per supercell. When adding holes into the $Fe_{In}$@mo system, the magnetic semiconductor to half-metallic nature transition, and *vice versa*, can be controlled by hole level. Our findings show that the electronic and magnetic properties of the pristine, defective, and Fe-doped InS monolayers can be effectively modified through hole doping, where the hole level may be a key role in obtaining the desirable features.

## 4.  Conclusions

In summary, first-principles calculations have been performed to investigate systematically the effects of vacancy defects and Fe doping, as well as further hole doping, on the InS monolayer's electronic and magnetic properties. The calculated phonon dispersion relations, AIMD simulations, and elastic constants confirm good stability for the InS monolayer. The band structure of the pristine monolayer is formed mainly by In-s–$p_{x,y,z}$ and S-$p_{x,y,z}$ states, which show significant hybridization to form covalent bonds. Moreover, the ionic character is also demonstrated for the In–S chemical bonds since the S atoms attract charge from the In atoms. The In–In bond is purely covalent. Significant monolayer magnetization is induced by creating In vacancies and doping with Fe atoms. In defective systems, S atoms around the doping site mainly produce the magnetic moment. Meanwhile the Fe impurity determines the magnetic properties of the Fe-doped InS monolayer. In these cases, feature-rich magnetic semiconductor and half-metallic natures are obtained, along with the in-plane magnetic anisotropy. Further hole doping can enhance significantly the magnetic properties of the $1Va_{In}$@mo system, but causes the disappearance of magnetism in the $2Va_{In}$@mo system. Interestingly, the nonmagnetic pristine InS and $1Va_2$@mo systems are magnetized with hole concentrations from 0.5 and 1.5 holes per supercell, respectively, giving place to the IMA. Importantly, hole doping is predicted to strengthen the IMA of the Fe-doped InS monolayer, however the total magnetic moment decreases increasing the hole level. Except for the $2Va_{In}$@mo system, the magnetic semiconducting to half-metallicity transition, and *vice versa*, can take place by properly controlling the hole concentration. Our results may suggest functionalization methods to make the InS monolayer a promising 2D platform for magnetic field sensing applications, where electronic and magnetic properties can be effectively controlled by hole doping.

## Conflicts of interest

The authors declare that they have no known competing financial interests or personal relationships that could have appeared to influence the work reported in this paper.

## Data availability

Data related to this study are available upon reasonable request.

## Acknowledgements

## References

1 K. S. Novoselov, A. K. Geim, S. V. Morozov, D.-E. Jiang, Y. Zhang, S. V. Dubonos, I. V. Grigorieva and A. A. Firsov, Electric field effect in atomically thin carbon films, *Science*, 2004, **306**(5696), 666–669.

2 A. K. Geim and K. S. Novoselov, The rise of graphene, *Nat. Mater.*, 2007, **6**(3), 183–191.

3 C. Soldano, A. Mahmood and E. Dujardin, Production, properties and potential of graphene, *Carbon*, 2010, **48**(8), 2127–2150.

4 X. Fan, Z. Shen, A. Liu and J.-L. Kuo, Band gap opening of graphene by doping small boron nitride domains, *Nanoscale*, 2012, **4**(6), 2157–2165.

5 J. E. Johns and M. C. Hersam, Atomic covalent functionalization of graphene, *Acc. Chem. Res.*, 2013, **46**(1), 77–86.

6 M. Y. Han, B. Özyilmaz, Y. Zhang and P. Kim, Energy band-gap engineering of graphene nanoribbons, *Phys. Rev. Lett.*, 2007, **98**(20), 206805.

7 Y.-W. Son, M. L. Cohen and S. G. Louie, Energy gaps in graphene nanoribbons, *Phys. Rev. Lett.*, 2006, **97**(21), 216803.

8 M. Chhowalla, Z. Liu and H. Zhang, Two-dimensional transition metal dichalcogenide (TMD) nanosheets, *Chem. Soc. Rev.*, 2015, **44**(9), 2584–2586.

9 B. Zhao, D. Shen, Z. Zhang, P. Lu, M. Hossain, J. Li, B. Li and X. Duan, 2D metallic transition-metal dichalcogenides: structures, synthesis, properties, and applications, *Adv. Funct. Mater.*, 2021, **31**(48), 2105132.

10 A. VahidMohammadi, J. Rosen and Y. Gogotsi, The world of two-dimensional carbides and nitrides (MXenes), *Science*, 2021, **372**(6547), eabf1581.

11 M. Naguib, V. N. Mochalin, M. W. Barsoum and Y. Gogotsi, 25th anniversary article: MXenes: a new family of two-dimensional materials, *Adv. Mater.*, 2014, **26**(7), 992–1005.

12 A. Carvalho, M. Wang, X. Zhu, A. S. Rodin, H. Su and A. H. Castro Neto, Phosphorene: from theory to applications, *Nat. Rev. Mater.*, 2016, **1**(11), 16061.

13 M. Pumera and Z. Sofer, 2D monoelemental arsenene, antimonene, and bismuthene: beyond black phosphorus, *Adv. Mater.*, 2017, **29**(21), 1605299.

14 H. Zheng, X.-B. Li, N.-K. Chen, S.-Y. Xie, W. Q. Tian, Y. Chen, H. Xia, S. Zhang and H.-B. Sun, Monolayer II-VI semiconductors: A first-principles prediction, *Phys. Rev. B:Condens. Matter Mater. Phys.*, 2015, **92**(11), 115307.

15 Y. Yang, Y. Yan, M. Sun, Y. Ma, Q. Chen and J. Z. Liu, Structural landscape of two-dimensional phases in group

II–VI semiconductors, *Appl. Phys. Lett.*, 2025, **127**(14), 142106.

16 S. Demirci, N. Avazlı, E. Durgun and S. Cahangirov, Structural and electronic properties of monolayer group III monochalcogenides, *Phys. Rev. B:Condens. Matter Mater. Phys.*, 2017, **95**(11), 115409.

17 Z. Yang and J. Hao, Recent progress in 2D layered III–VI semiconductors and their heterostructures for optoelectronic device applications, *Adv. Mater. Technol.*, 2019, **4**(8), 1900108.

18 L. Zhao, B. Wang and R. Wang, A critical review on new and efficient 2D materials for catalysis, *Adv. Mater. Interfaces*, 2022, **9**(29), 2200771.

19 D. Deng, K. Novoselov, Q. Fu, N. Zheng, Z. Tian and X. Bao, Catalysis with two-dimensional materials and their heterostructures, *Nat. Nanotechnol.*, 2016, **11**(3), 218–230.

20 J. S. Ponraj, Z.-Q. Xu, S. C. Dhanabalan, H. Mu, Y. Wang, J. Yuan, P. Li, S. Thakur, M. Ashrafi, K. Mccoubrey, *et al.*, Photonics and optoelectronics of two-dimensional materials beyond graphene, *Nanotechnology*, 2016, **27**(46), 462001.

21 Q. H. Wang, K. Kalantar-Zadeh, A. Kis, J. N. Coleman and M. S. Strano, Electronics and optoelectronics of two-dimensional transition metal dichalcogenides, *Nat. Nanotechnol.*, 2012, **7**(11), 699–712.

22 L. Wang, L. Huang, W. C. Tan, X. Feng, L. Chen, X. Huang and K.-W. Ang, 2D photovoltaic devices: progress and prospects, *Small Methods*, 2018, **2**(3), 1700294.

23 S. Das, D. Pandey, J. Thomas and T. Roy, The role of graphene and other 2D materials in solar photovoltaics, *Adv. Mater.*, 2019, **31**(1), 1802722.

24 Y. Xue, Q. Zhang, W. Wang, H. Cao, Q. Yang and L. Fu, Opening two-dimensional materials for energy conversion and storage: a concept, *Adv. Energy Mater.*, 2017, **7**(19), 1602684.

25 X. Zhang, L. Hou, A. Ciesielski and P. Samorì, 2D materials beyond graphene for high-performance energy storage applications, *Adv. Energy Mater.*, 2016, **6**(23), 1600671.

26 Y. Liu, C. Zeng, J. Zhong, J. Ding, Z. M. Wang and Z. Liu, Spintronics in two-dimensional materials, *Nano-Micro Lett.*, 2020, **12**(1), 93.

27 I. Choudhuri, P. Bhauriyal and B. Pathak, Recent advances in graphene-like 2D materials for spintronics applications, *Chem. Mater.*, 2019, **31**(20), 8260–8285.

28 G. W. Mudd, S. A. Svatek, T. Ren, A. Patanè, O. Makarovsky, L. Eaves, P. H. Beton, Z. D. Kovalyuk, G. V. Lashkarev, Z. R. Kudrynskyi, *et al.*, Tuning the bandgap of exfoliated InSe nanosheets by quantum confinement, *Adv. Mater.*, 2013, **25**(40), 5714.

29 D. Hlushchenko, A. Siudzinska, J. Cybinska, M. Guzik, A. Bachmatiuk and R. Kudrawiec, Stability of mechanically exfoliated layered monochalcogenides under ambient conditions, *Sci. Rep.*, 2023, **13**(1), 19114.

30 H.-C. Chang, C.-L. Tu, K.-I. Lin, J. Pu, T. Takenobu, C.-N. Hsiao and C.-H. Chen, Synthesis of large-area InSe monolayers by chemical vapor deposition, *Small*, 2018, **14**(39), 1802351.

31 T. Afaneh, A. Fryer, Y. Xin, R. H. Hyde, N. Kapuruge and H. R. Gutierrez, Large-area growth and stability of monolayer gallium monochalcogenides for optoelectronic devices, *ACS Appl. Nano Mater.*, 2020, **3**(8), 7879–7887.

32 H. Wang, G. Qin, J. Yang, Z. Qin, Y. Yao, Q. Wang and M. Hu, First-principles study of electronic, optical and thermal transport properties of group III–VI monolayer MX (M = Ga, In; X = S, Se), *J. Appl. Phys.*, 2019, **125**(24), 245104.

33 C.-L. Tu, K.-I. Lin, J. Pu, T.-F. Chung, C.-N. Hsiao, A.-C. Huang, J.-R. Yang, T. Takenobu and C.-H. Chen, CVD growth of large-area InS atomic layers and device applications, *Nanoscale*, 2020, **12**(17), 9366–9374.

34 J. Jalilian and M. Safari, Electronic and optical properties of *α*-InX (X = S, Se and Te) monolayer: Under strain conditions, *Phys. Lett. A*, 2017, **381**(15), 1313–1320.

35 H. Jin, J. Li, Y. Dai and Y. Wei, Engineering the electronic and optoelectronic properties of InX (X = S, Se, Te) monolayers via strain, *Phys. Chem. Chem. Phys.*, 2017, **19**(6), 4855–4860.

36 H. Jin, J. Li, B. Wang, Y. Yu, L. Wan, F. Xu, Y. Dai, Y. Wei and H. Guo, Electronics and optoelectronics of lateral heterostructures within monolayer indium monochalcogenides, *J. Mater. Chem. C*, 2016, **4**(47), 11253–11260.

37 A. Rawat, R. Ahammed, Dimple, N. Jena, M. K. Mohanta and A. De Sarkar, Solar energy harvesting in type II van der Waals heterostructures of semiconducting group III monochalcogenide monolayers, *J. Phys. Chem. C.*, 2019, **123**(20), 12666–12675.

38 R. Xue, R. Han, X. Lin and P. Wu, First-principles investigate on the electronic structure and magnetic properties of 3d transition metal doped honeycomb InS monolayer, *Appl. Surf. Sci.*, 2023, **608**, 155240.

39 B. Xu, L. Zuo, W. Zhao, Q. Yang, Y. Wang, M. Zhang, L. Yi, *et al.*, Prediction of magnetic properties of 3d transition-metal adsorbed InS monolayers, *J. Magn. Magn. Mater.*, 2024, **603**, 172241.

40 L. Ao, H. Xiao, X. Xiang, S. Li, K. Liu, H. Huang and X. Zu, Functionalization of a GaSe monolayer by vacancy and chemical element doping, *Phys. Chem. Chem. Phys.*, 2015, **17**(16), 10737–10748.

41 D. Hoat, N. T. Tien, D. K. Nguyen and J. Guerrero-Sanchez, Antiferromagnetism in gas monolayer doped with TM–TM atom pairs (TM = V, Cr, Mn, and Fe), *Phys. Chem. Chem. Phys.*, 2024, **26**(27), 18657–18666.

42 R. Meng, M. Houssa, K. Iordanidou, G. Pourtois, V. Afanasiev and A. Stesmans, Ferromagnetism and half-metallicity in two-dimensional MO (M = Ga, In) monolayers induced by hole doping, *Phys. Rev. Mater.*, 2020, **4**(7), 074001.

43 T. Cao, Z. Li and S. G. Louie, Tunable magnetism and half-metallicity in hole-doped monolayer GaSe, *Phys. Rev. Lett.*, 2015, **114**(23), 236602.

44 W. Kohn and L. J. Sham, Self-consistent equations including exchange and correlation effects, *Phys. Rev.*, 1965, **140**(4A), A1133, DOI: 10.1103/PhysRev.140.A1133.

45 G. Kresse and J. Furthmüller, Efficiency of ab-initio total energy calculations for metals and semiconductors using

a plane-wave basis set, *Comput. Mater. Sci.*, 1996, **6**(1), 15–50, DOI: 10.1016/0927-0256(96)00008-0.

46 G. Kresse and J. Furthmüller, Efficient iterative schemes for ab initio total-energy calculations using a plane-wave basis set, *Phys. Rev. B:Condens. Matter Mater. Phys.*, 1996, **54**(16), 11169, DOI: 10.1103/PhysRevB.54.11169.

47 J. P. Perdew, K. Burke and M. Ernzerhof, Generalized gradient approximation made simple, *Phys. Rev. Lett.*, 1996, **77**(18), 3865, DOI: 10.1103/PhysRevLett.77.3865.

48 S. L. Dudarev, G. A. Botton, S. Y. Savrasov, C. Humphreys and A. P. Sutton, Electron-energy-loss spectra and the structural stability of nickel oxide: An LSDA+U study, *Phys. Rev. B:Condens. Matter Mater. Phys.*, 1998, **57**(3), 1505.

49 Y. Wang, S. Li and J. Yi, Transition metal-doped tin monoxide monolayer: a first-principles study, *J. Phys. Chem. C.*, 2018, **122**(8), 4651–4661.

50 H. J. Monkhorst and J. D. Pack, Special points for Brillouin-zone integrations, *Phys. Rev. B: Condens. Matter Mater. Phys.*, 1976, **13**(12), 5188, DOI: 10.1103/PhysRevB.13.5188.

51 A. Singh and A. K. Singh, Origin of n-type conductivity of monolayer MoS$_2$, *Phys. Rev. B*, 2019, **99**(12), 121201.

52 J. Zhang, Y. Liu, C. Yang, Y. Qu, A. Zhang, Z. Feng, W. Wang and P. Ou, Design of bifunctional oxygen evolution/reduction electrocatalysts on g-C$_3$N$_3$ monolayer by a defect physics method, *J. Catal.*, 2025, **447**, 116135.

53 C. Yang, C. Yang, Y. Liang, H. Yan, A. Zhang, G. Ge, W. Wang and P. Ou, Machine-learning enables nitrogen reduction reaction on transition metal doped C$_3$B by controlling the charge states, *Mater. Chem. Front.*, 2025, **9**(11), 1681–1689.

54 S. Yue, D. Li, A. Zhang, Y. Yan, H. Yan, Z. Feng and W. Wang, Rational design of single transition-metal atoms anchored on a PtSe$_2$ monolayer as bifunctional OER/ORR

55 W. Wentao, Y. Qu, D. Li, A. Zhang, H. Yan, Z. Feng and W. Yao, The defect chemistry and machine learning study 5d transition metal doped on graphitic carbon nitride for bifunctional oxygen electrocatalyst with low overpotential, *Int. J. Hydrogen Energy*, 2024, **79**, 702–714.

56 H.-P. Komsa, N. Berseneva, A. V. Krasheninnikov and R. M. Nieminen, Charged point defects in the flatland: Accurate formation energy calculations in two-dimensional materials, *Phys. Rev. X*, 2014, **4**(3), 031044.

57 A. S. Nissimagoudar, Z. Rashid, J. Ma and W. Li, Lattice thermal transport in monolayer group 13 monochalcogenides MX (M = Ga, In; X = S, Se, Te): Interplay of atomic mass, harmonicity, and lone-pair-induced anharmonicity, *Inorg. Chem.*, 2020, **59**(20), 14899–14909.

58 A. Togo, L. Chaput, T. Tadano and I. Tanaka, Implementation strategies in phonopy and phono3py, *J. Phys. Condens. Matter*, 2023, **35**(35), 353001, DOI: 10.1088/1361-648X/acd831.

59 S. Nosé, A unified formulation of the constant temperature molecular dynamics methods, *J. Chem. Phys.*, 1984, **81**(1), 511–519.

60 W. G. Hoover, Canonical dynamics: Equilibrium phase-space distributions, *Phys. Rev.*, 1985, **31**(3), 1695.

61 F. Mouhat and F.-X. Coudert, Necessary and sufficient elastic stability conditions in various crystal systems, *Phys. Rev. B: Condens. Matter Mater. Phys.*, 2014, **90**(22), 224104.

62 A. V. Krukau, O. A. Vydrov, A. F. Izmaylov and G. E. Scuseria, Influence of the exchange screening parameter on the performance of screened hybrid functionals, *J. Chem. Phys.*, 2006, **125**(22), 224106.

54 (continued) electrocatalysts: a defect chemistry and machine learning study, *J. Mater. Chem. A*, 2024, **12**(9), 5451–5463.